Modelling, bifurcation analysis, circuit design and FPGA-based implementation of a new chaotic jerk system exhibiting Hopf bifurcations

Sundarapandian Vaidyanathan*

Centre for Control Systems, Vel Tech University
400 Feet Outer Ring Road, Avadi, Chennai-600062
Tamil Nadu, India
E-mail: sundarcontrol@gmail.com
*Corresponding author

Irene M. Moroz

Mathematical Institute, University of Oxford
Oxford OX2 6GG, England, UK
E-mail: Irene.Moroz@maths.ox.ac.uk

Aceng Sambas

Faculty of Informatics and Computing
Universiti Sultan Zainal Abidin
Kampung Gong Badak, 21300
Terengganu, Malaysia
and
Department of Mechanical Engineering
Universitas Muhammadiyah Tasikmalaya
Tasikmalaya 46196, West Java
Indonesia
E-mail: acengs@umtas.ac.id

Daniel Clemente-Lopez

Digital Systems Group, Department of Electronics
Instituto Nacional de Astrofísica, Óptica y Electrónica (INAOE)
Tonantzintila, Puebla 72840, Mexico
E-mail: daniel.clemente@inaoep.mx

Jesus M. Munoz-Pacheco

Faculty of Electronics Sciences
Benemérita Universidad Autónoma de Puebla
4 Sur 104, Colonia Centro, C.P. 72000, Puebla, Mexico
E-mail: jesusm.pacheco@correo.buap.mx

Jose de Jesus Rangel-Magdaleno

Digital Systems Group, Department of Electronics
Instituto Nacional de Astrofísica, Óptica y Electrónica (INAOE)
Tonantzintila, Puebla 72840, Mexico
E-mail: jrangel@inaoe.mx

Abstract: It is well-known that chaotic systems have several applications in scientific modelling and engineering fields such as encryption, cryptosystems, secure communication, etc. This work proposes a three-dimensional mechanical chaotic system with jerk dynamics. A detailed bifurcation analysis is conducted for the proposed chaotic system. It is shown that the proposed chaotic system has two equilibrium points which exhibit Hopf bifurcations. It is also shown that the proposed chaotic system depicts multistability and coexisting chaotic attractors. Using Multisim (Version 14), an electronic circuit is designed for the proposed mechanical chaotic system with jerk dynamics. As another engineering application, Field Programmable Gate Array (FPGA) design has been made for the proposed mechanical jerk chaotic system. Euler's finite-difference method is used for our FPGA design. A hardware implementation of the FPGA-based design is performed in this work and experimental results are given in detail.

1 Introduction

In the recent years, significant developments have been carried out in various applications of modelling and engineering applications of various dynamical systems (Li and Sun, 2023; Liu and Chang, 2023; Wang and Cheng, 2021; Liu and Wang, 2023; Li and Ye, 2023; Bors and Stańczy, 2023; Yu and Zhang, 2023; Das and Mohanty, 2022a; Arowolo et al., 2022; Dilna et al., 2022; Patro et al., 2022; Das and Mohanty, 2022b; Wang et al., 2022; Hassani et al., 2022; Owais and Iqbal, 2022). Chaos theory dealing with the modelling and applications of chaotic dynamical systems has wide applications such as memristors (Chen and Min, 2022; Singh and Rai, 2022; Cao and Lai, 2022), cryptosystems (Sachin and Singh, 2022; Anandkumar and Kalpana, 2022; Shafique, 2022), neural networks (Farlessyost and Singh, 2022; Samuilik and Sadyrbaev, 2023; Wang and Guet, 2022), chemical reactors (Thounaojam, 2022; Ryashko, 2022), finance (Wang and Yang, 2021; Xu, 2022), etc.

Mechanical dynamical systems have a variety of applications of science and engineering (Nagase and Taniuchi, 2023; Zhen and Hongbao, 2023; Mastrone and Co, 2023; Sui and Zhang, 2023; Shafaei and Mousazadeh, 2023; Wu and Chen, 2023; Guo and Li, 2023).

In classical mechanics, an autonomous jerk differential equation is given by a third order ODE having the general form

$$\dddot{\xi} = F(\xi, \dot{\xi}, \ddot{\xi}) \tag{1}$$

In mechanical engineering, the third derivative has the physical interpretation of "*jerk*" of a displacement, while the second derivative has the physical interpretation of "*acceleration*".

Using the phase variables defined by

$$z_1 = \xi,\ z_2 = \dot{\xi}, z_3 = \ddot{\xi}, \tag{2}$$

we can represent the autonomous jerk ODE (1) equivalently as

$$\begin{cases} \dot{z}_1 = z_2 \\ \dot{z}_2 = z_3 \\ \dot{z}_3 = F(z_1, z_2, z_3) \end{cases} \tag{3}$$

In the recent years, chaotic jerk systems are studied by several researchers (Vaidyanathan et al., 2018; Kengne et al., 2022; Rech, 2022; Tagne et al., 2022). In this research paper, we propose a new 3-D jerk system possessing 3 quadratic nonlinear terms and dissipative chaotic motion. In chaos theory, bifurcation analysis is applied to develop insights into qualitative behaviour of various chaotic systems (Han and Lei, 2023; Gupta et al., 2023; Li and Cui, 2023; Al-Basyouni and Khan, 2022).

An innovative feature of our jerk system is that it exhibits Hopf bifurcations associated with the two equilibrium points. In the bifurcation theory of nonlinear dynamical systems, the existence or the disappearance of a limit cycle through a local change in the stability properties of a balance point is a local bifurcation called as the *Hopf bifurcation* (Guckenheimer and Holmes, 1983). The new jerk system also exhibits multistability with coexisting chaotic attractors, where multistability refers to coexistence of two or more chaotic attractors for the same parameter set but different initial states (Dong et al., 2022; Ostrovskii et al., 2022).

Using Multisim (Verion 14), we develop an electronic circuit of the proposed jerk system. It is noted that electronic and experimental circuit designs of chaotic systems enable real-world implementations of the underlying systems in various engineering applications (Xu and Zhang, 2022; Zhang and Li, 2022; Mao and Lei, 2022).

Field Programmable Gate Arrays (FPGAs) have many applications in science and engineering (Törk, 2022; Gupta and Chauhan, 2022; Abdullah and Mohammed, 2022). It is well-known that FPGAs can be reprogrammed so as to suit any desired application or functionality requirements after manufacturing. In this research work, FPGA design has been made for the proposed mechanical jerk chaotic system. Euler's finite-difference method is used for our FPGA design. A hardware implementation of the FPGA-based design is performed in this work and experimental results are given in detail.

2 A new jerk dynamics with a chaotic attractor

We propose the new 3-D jerk dynamics

$$\begin{cases} \dot{z}_1 = z_2 \\ \dot{z}_2 = z_3 \\ \dot{z}_3 = -az_1 + bz_2 - z_3 - cz_1^2 - z_1z_2 + dz_2^2 \end{cases} \tag{4}$$

We observe that the constants a, b and c in Eq. (4) are assumed to be positive. We denote the state of the jerk dynamics (4) as $Z = (z_1, z_2, z_3)$.

For MATLAB simulations, we take the initial state as $Z(0) = (0.4, 0.1, 0.4)$ and the constants as $(a, b, c, d) = (1, 0.2, 0.2, 1)$.

For this data set, the Lyapunov Exponents (LE) of the model (4) were computed numerically in MATLAB for $T = 1E5$ seconds as follows:

$$\tau_1 = 0.1542, \tau_2 = 0, \tau_3 = -1.1542. \tag{5}$$

The Kaplan-Yorke fractal chaotic dimension of the jerk model (4) is computed as given below:

$$D_K = 2 + \frac{\tau_1 + \tau_2}{|\tau_3|} = 2.1336 \tag{6}$$

Since the largest Lyapunov exponent (LLE) has a positive value ($\tau_1 > 0$), we deduce that the dynamics (4) has a chaotic attractor.

We note that

$$\tau_1 + \tau_2 + \tau_3 = -1. \tag{7}$$

Since the sum of the three LE values of the jerk system (4) is negative, we deduce that the chaotic motion of the jerk system (4) is dissipative.

In order to find the equilibrium points of the jerk system (4), we solve the following system of equations:

$$z_2 = 0 \quad (8a)$$

$$z_3 = 0 \quad (8b)$$

$$-az_1 + bz_2 - z_3 - cz_1^2 - z_1z_2 + dz_2^2 = 0 \quad (8c)$$

From (8a) and (8b), we get $z_2 = 0$ and $z_3 = 0$.

Substituting these values into Eq. (8c), we get

$$-az_1 - cz_1^2 = 0 \quad \text{or} \quad -z_1(a + cz_1) = 0 \quad (9)$$

This shows that $z_1 = 0$ or $z_1 = -\frac{a}{c}$.

Thus, there are two equilibrium points for the jerk system (4) given by

$$Z_0 = \begin{bmatrix} 0 \\ 0 \\ 0 \end{bmatrix} \quad \text{and} \quad Z_1 = \begin{bmatrix} -\frac{a}{c} \\ 0 \\ 0 \end{bmatrix} \quad (10)$$

The linearisation matrix for the jerk system (4) at Z_0 has the following spectral values:

$$\lambda_1 = -1.5471, \ \lambda_{2,3} = 0.2735 \pm 0.7560i \quad (11)$$

This spectral calculation shows that the jerk system (4) has a *saddle-focus* equilibrium at Z_0, which is unstable.

The linearisation matrix for the jerk system (4) at Z_1 has the following spectral values:

$$\lambda_1 = -2.7555, \ \lambda_2 = -0.1868, \lambda_3 = \ 1.9423 \quad (12)$$

This spectral calculation shows that the jerk system (4) has a *saddle-point* equilibrium at Z_1, which is unstable.

The new jerk system (4) has a *self-excited* chaotic attractor and this is due to the fact that the jerk system (4) possesses a finite number of unstable equilibrium points (Vaidyanathan et al., 2018).

MATLAB simulations showing 2-D projections of the chaotic attractor of the jerk system (4) are exhibited in Figures 1, 2 and 3.

Figures 4-5 show the multi-stability property of the new chaotic jerk system (4) where the blue orbits correspond to $Z_0 = (0.4, 0.1, 0.4)$, while the red orbits correspond to $W_0 = (-0.8, 0.1, -0.8)$.

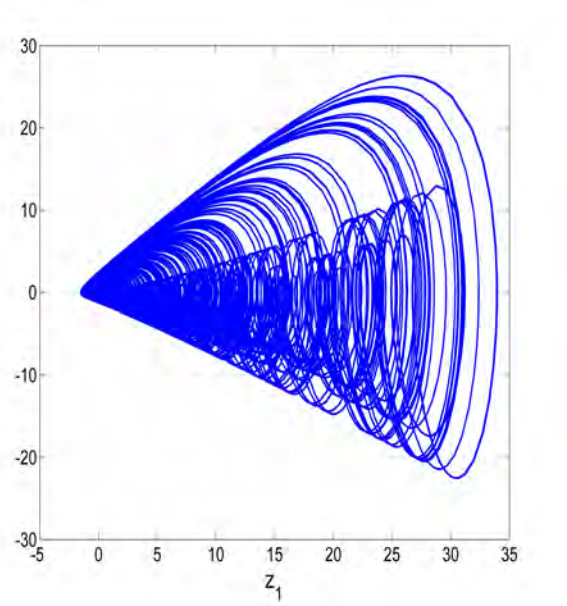

Figure 1: Signal plot for the 3-D chaotic jerk system (4) in the (z_1, z_2) plane for $Z(0) = (0.4, 0.1, 0.4)$ and $(a, b, c, d) = (1, 0.2, 0.2, 1)$.

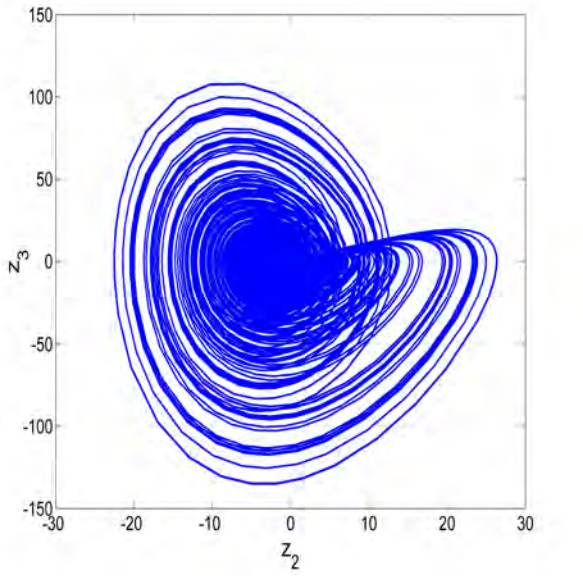

Figure 2: Signal plot for the 3-D chaotic jerk system (4) in the (z_1, z_2) plane for $Z(0) = (0.4, 0.1, 0.4)$ and $(a, b, c, d) = (1, 0.2, 0.2, 1)$.

3 Bifurcation analysis of the new jerk system

3.1 The jerk system

The new 3-D jerk system (4) can be expressed as follows:

$$\begin{cases} \dot{x} = y \\ \dot{y} = z \\ \dot{z} = -ax + by - z - cx^2 - xy + dy^2 \end{cases} \quad (13)$$

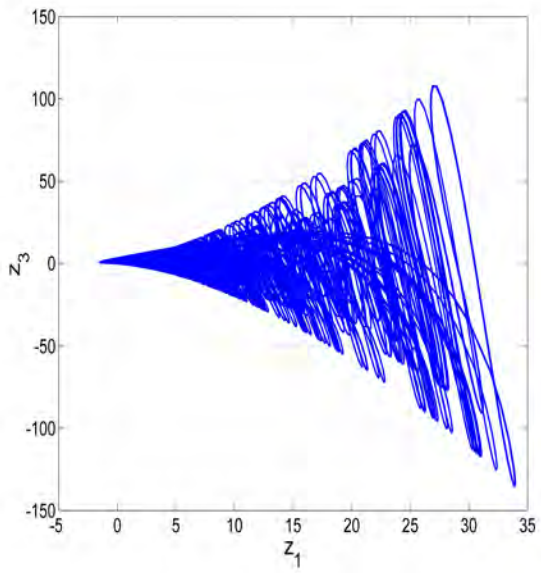

Figure 3: Signal plot for the 3-D chaotic jerk system (4) in the (z_1, z_2) plane for $Z(0) = (0.4, 0.1, 0.4)$ and $(a, b, c, d) = (1, 0.2, 0.2, 1)$.

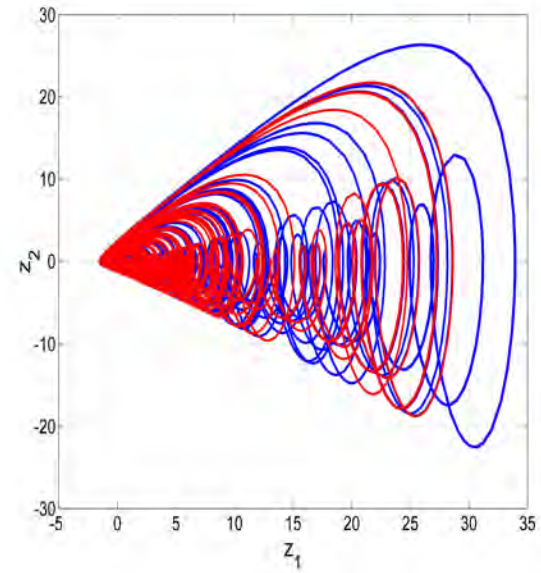

Figure 4: Multi-stability property of the new jerk system (4) is observed in (z_1, z_2)-plane for $(a, b, c, d) = (1, 0.2, 0.2, 1)$ and the initial states $Z_0 = (0.4, 0.1, 0.4)$ and $W_0 = (-0.8, 0.1, -0.8)$, where the blue orbit corresponds to Z_0 and the red orbit corresponds to W_0.

It is convenient to represent the state of (13) as $X = (x, y, z)$.

Although the chosen set of parameter values is $(a, b, c, d) = (1, 0.2, 0.2, 1)$, we explore the dynamics of system (13) in the neighbourhood of these parameter values to get an indication of possible bifurcations.

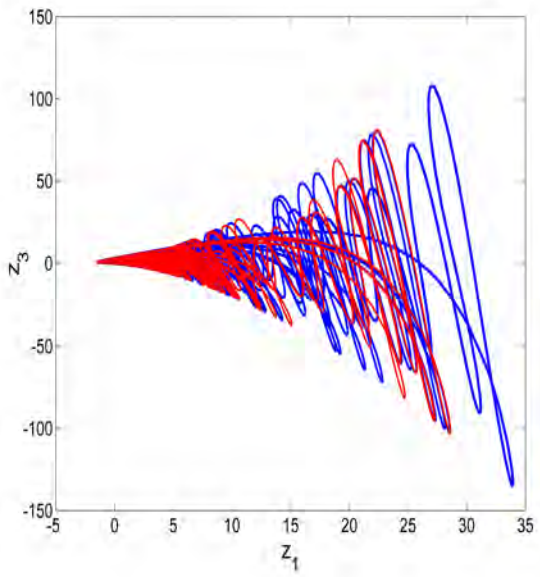

Figure 5: Multi-stability property of the new jerk system (4) is observed in (z_1, z_3)-plane for $(a, b, c, d) = (1, 0.2, 0.2, 1)$ and the initial states $Z_0 = (0.4, 0.1, 0.4)$ and $W_0 = (-0.8, 0.1, -0.8)$, where the blue orbit corresponds to Z_0 and the red orbit corresponds to W_0.

As shown in Section 2, the jerk system (13) has a trivial equilibrium $X_0 = (0, 0, 0)$ and a nontrivial equilibrium $X_e = \left(-\frac{a}{c}, 0, 0\right)$.

The linear stability of each fixed point is determined from the characteristic polynomial.

We first compute the Jacobian matrix:

$$J = \begin{pmatrix} 0 & 1 & 0 \\ 0 & 0 & 1 \\ -(a + 2cx + y) & b - (x + 2dy) & -1 \end{pmatrix}. \tag{14}$$

The characteristic equation is then obtained from the determinant of $J - \lambda I_3$, evaluated at each equilibrium state where λ are the eigenvalues and I_3 is the $(3, 3)$ identity matrix.

(i) For the equilibrium point X_0, we obtain the cubic characteristic equation:

$$\lambda^3 + \lambda^2 - \lambda b + a = 0. \tag{15}$$

(ii) For the equilibrium point X_e, we obtain the cubic characteristic equation:

$$\lambda^3 + \lambda^2 - \lambda \left(b + \frac{a}{c}\right) - a = 0. \tag{16}$$

3.2 Bifurcations

We now try to identify the possible bifurcations that can arise for general parameter values.

3.2.1 Trivial equilibrium state X_0

A steady state bifurcation ($\lambda = 0$) occurs when $a = 0$; the remaining two eigenvalues being

$$\lambda = \frac{1}{2}(-1 \pm \sqrt{[1 + 4b]}). \tag{17}$$

Both eigenvalues are real for $b > -1/4$. If $b > 0$, we have a saddle point; if $0 > b > -1/4$ we have a stable node; and when $-1/4 > b$ we have a stable focus.

If $a = 0 = b$, we have a codimension-two double zero bifurcation, the third eigenvalue being $\lambda = -1$.

A Hopf bifurcation is possible when $\lambda = \pm\imath\omega$, when $a + b = 0$, provided $a > 0$ and $b < 0$, with frequency given by $\omega = \sqrt{a}$.

3.2.2 Nontrivial equilibrium state X_e

Again the simple form for the characteristic equation (16) means we can immediately write down the criteria for steady state, double-zero and Hopf bifurcations.

A steady-state bifurcation occurs when $a = 0$. This reduces the characteristic equation to the same form as for the trivial equilibrium point. The results for that fixed point therefore hold for the nontrivial fixed point.

The same is also true for the double-zero bifurcation, where we again require $a = b = 0$. This coincidence is because the nontrivial fixed point is distinguished from the trivial fixed point for $a \neq 0$.

A Hopf bifurcation for the nontrivial fixed point is possible along the curve

$$a_{HE} = \frac{b}{1 - \frac{1}{c}} \tag{18}$$

provided $a < 0$ with frequency $\Omega = \sqrt{-a}$. Since a_{HE} also depends upon the parameter c, if $c < 1$ (as is the case for the chosen value of $c = 0.2$), then $a < 0$ implies that we require $b > 0$. (On the other hand, if $c > 1$, then we must also have $b < 0$.)

Figure 6 shows the linear stability curves in the (b, a)-plane for both the trivial and nontrivial equilibrium states for the case of $c < 1$ (since we chose $c = 0.2$ for this study). The stable steady state bifurcation for both trivial and nontrivial equilibria (SS) is shown as the solid black curve, while the unstable portion is the dashed black curve. The Hopf bifurcation for the trivial equilibrium is the blue curve (HB0), while that for the nontrivial equilibrium is shown in red (as HBE). All curves intersect in the double-zero bifurcation, labelled 'DZ'.

Figure 7 shows the eigenspectra for both the trivial and nontrivial fixed points in for $a = 0.2$ in $-1 \leq b \leq 1$. The blue curve tracks the real eigenvalue for the trivial fixed point and the black curve tracks the real part of the complex conjugate eigenvalues. The green and magenta curves track the corresponding eigenvalues for the nontrivial state. The trivial fixed point is stable whenever the blue and black curves lie in the lower half plane, while the nontrivial fixed point is stable whenever the green and magenta curves lie in the lower half plane. In Figure 7, the blue curve tracks the real eigenvalue and the black curve tracks the real part of the complex eigenvalues for the trivial equilibrium state. The green curve tracks the real eigenvalue and the magenta curve tracks the real part of the complex eigenvalue for the nontrivial equilibrium state. The trivial state undergoes

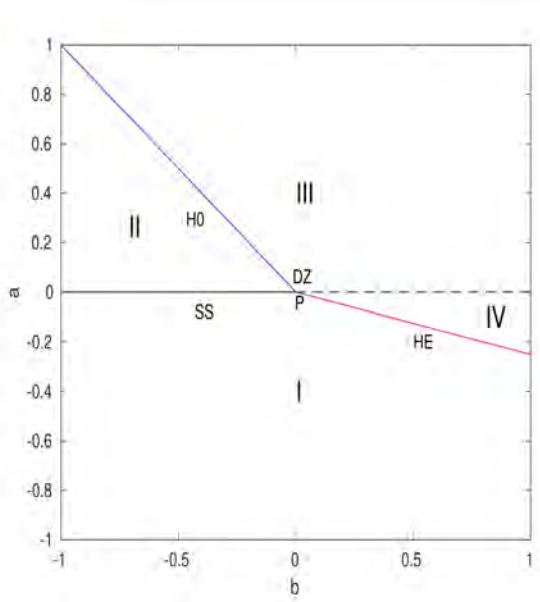

Figure 6: The linear stability curves for the trivial and nontrivial fixed points in the (b, a)-plane for $c = 0.2$ and $d = 1$.

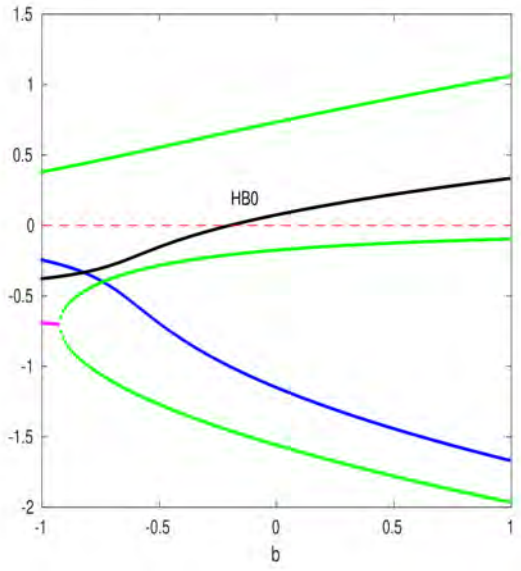

Figure 7: The linear eigenspectra for the trivial and nontrivial equilibrium states for $-1 \leq b \leq 1$ and $a = 0.2$.

a Hopf bifurcation ($HB0$) at $b = -0.2$ with frequency $\omega = 0.4491$, when the black curve crosses zero (the red dashed line).

We see that the trivial state undergoes a Hopf bifurcation at $b = -0.2$ with corresponding frequency $\omega = 0.4491$. For $-1 \leq b < -0.2$, the trivial state is a stable focus, becoming an unstable focus for $b > -0.2$. The nontrivial state is either an unstable saddle-focus for $-1 \leq b < -0.93$, or a saddle for $b > -0.93$.

Figure 8 shows the corresponding linear stability curves for $a = -0.2$. Now it is the nontrivial state that

undergoes a Hopf bifurcation along the curve $a_{HE} = b/(1-1/c)$. In Figure 8, the blue curve tracks the real eigenvalue and the black curve tracks the real part of the complex eigenvalues for the trivial equilibrium state. The green curve tracks the real eigenvalue and the magenta curve tracks the real part of the complex eigenvalue for the nontrivial equilibrium state. The nontrivial state undergoes a Hopf bifurcation (HBE) at $b = 0.8$ with frequency $\Omega = 0.44721$, when the magenta curve crosses the zero red dashed line).

The trivial state is unstable in $-1 \leq b \leq 1$, being either a saddle-focus for $-1 \leq b < -0.07$, or a saddle for $-0.07 < b \leq 1$. The nontrivial state is stable for $-1 \leq b < 0.8$, before losing stability to a Hopf bifurcation, labelled as HBE.

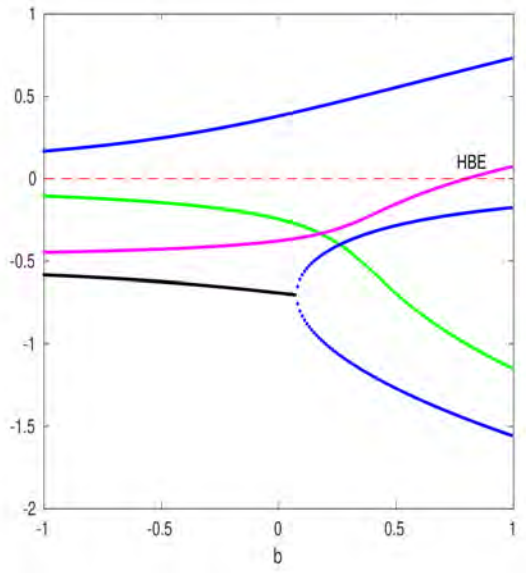

Figure 8: The linear eigenspectra for the trivial and nontrivial equilibrium states for $-1 \leq b \leq 1$ and $a = -0.2$.

3.3 Normal Forms

Another nonlinear 3-D system, describing the dynamics of a homopolar Faraday disk dynamo, has very similar linear stability curves (Hide et al., 1996). Unlike our system, there are 3 fixed points: a trivial and two nontrivial states (because of reflectional symmetry). Like our system, all 3 states share the same steady state curves and double-zero bifurcation points. There are two Hopf curves: using the notation in (Hide et al., 1996), a curve h_1 of Hopf bifurcations for the trivial state, and a curve h_2 for the nontrivial state. The former represents a supercritical Hopf bifurcation, while the latter is subcritical.

Our system does not exhibit reflectional symmetry, and so the appropriate normal form for the double-zero point is calculated as in (Guckenheimer and Holmes, 1983).

$$\begin{aligned} \dot{u} &= v, \\ \dot{v} &= \mu_1 + \mu_2 y + Au^2 + Buv, \end{aligned} \tag{19}$$

where $B = \pm 1$. The two bifurcation parameters are μ_1 and μ_2. These two parameters are linear combinations of small perturbations of our two bifurcation parameters a and b in the neighbourhood of the double-zero P. A local analysis of Eq. (19) gives two equilibria, one of which is a saddle and the other gives rise to a Hopf bifurcation. In the (μ_1, μ_2)-parameter plane, the curve of Hopf bifurcations is given by $\mu_1 = -{\mu_2}^2$, for $\mu_1 < 0$. The curve of saddle-node bifurcations occurs on $\mu_1 = 0$ for $\mu_2 \neq 0$. The limit cycle, born from the Hopf bifurcation, is destroyed in a homoclinic bifurcation on the curve $\mu_1 = -\frac{49}{25}{\mu_2}^2$, for $\mu_1 < 0$. This curve is computed through a Melnikov analysis, by writing Eq. (19) as a perturbed Hamiltonian system. Once the limit cycle is destroyed, the phase trajectories diverge. This is borne out in our numerical integrations of the original 3-D system (13), when trajectories diverge to infinity.

Our numerical integrations will show if $H0$ is a supercritical Hopf bifurcation, and HE is subcritical. In order to confirm this analytically, we would have to derive the centre manifolds and then the normal forms for the two Hopf bifurcations from eqns 1.1 for each fixed point.

Instead of following that procedure, here we choose to explore the dynamics local to, as well as further away from DZ.

3.4 Numerical Integrations

Figure 9 shows a traversal of the (b, a)-parameter space of Figure 1 in an anti-clockwise sense through the 4 regions labelled. In region I we find only stable steady states $\mathbf{x_e}$, as confirmed by the linear eigenspectra shown in Figure 8. The trivial state $\mathbf{x_0}$ is unstable for $a = -0.2$, while the nontrivial state is stable. In Figure 9 (a), we set $b = -0.2$ and increased a to $a = 1$. For $a = 0.2$, we now have a stable trivial state in region II, until we cross the Hopf bifurcation curve $H0$, where there is a finite amplitude transition at $a = 0.32$ to stable oscillations. (Decreasing a across the curve $H0$ from region III, but not shown here, we found hysteresis near the Hopf boundary and a termination of the periodic state at $a = 0.198$.) Next we set $a = 1$ and decreased b in $-1.0 \leq b \leq 0.2$, when the trajectories became unbounded. This bifurcation transition diagram is shown in Figure 9 (b). Then, with $b = 0.2$, we reduced a from $a = 1$ (Figure 9 (c)). We found chaotic dynamics before the trajectories again became unbounded at $a = 0.714$. Finally we set $a = -0.2$ and decreased b from $b = 1.0$ to obtain the bifurcation transition diagram of Figure 9 (d). The periodic solution terminates at $b = 0.8$ in a Hopf bifurcation for the nontrivial state. For $b < 0.8$, we have the stable nontrivial equilibrium state $x_e = 1$.

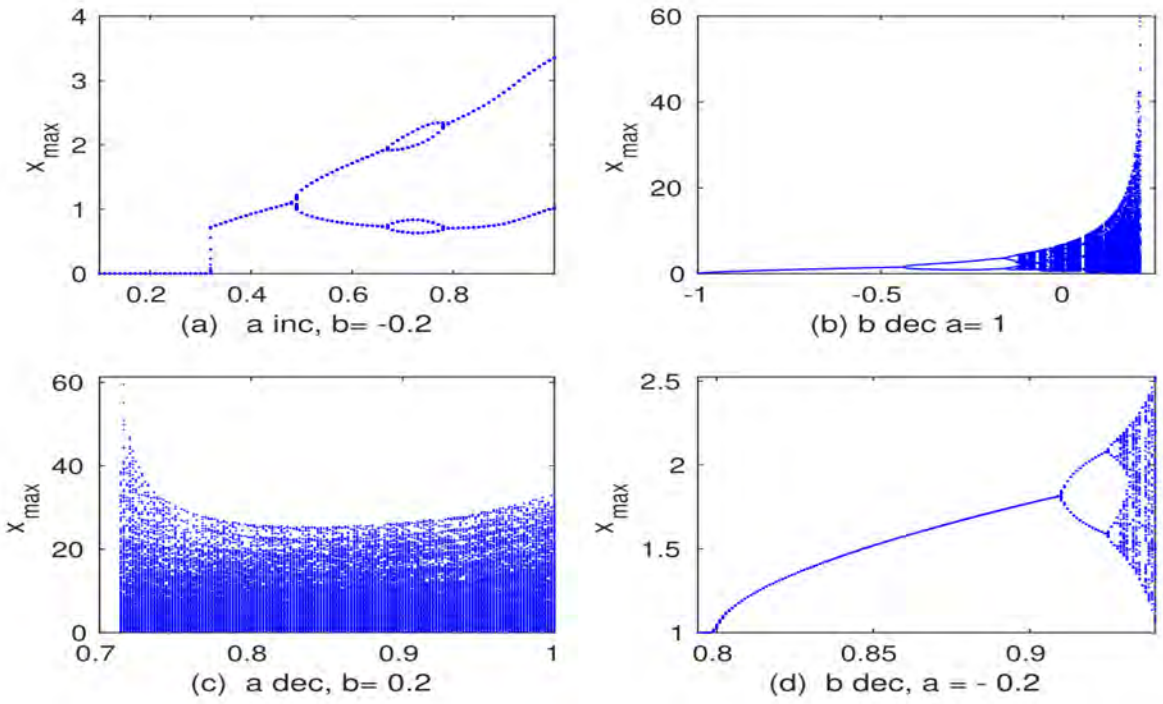

Figure 9: The bifurcation transition plots of x_{max} as a varies for $0 \leq a \leq 2.5$, initial state $X(0) = (0.4, 0.1, 0.4)$. Clearly shown are two separate chaotic and periodic regions.

4 Multisim model of the new 3D chaotic system with jerk dynamics

We use Multisim (Version 14) for the electronic design of the proposed system with jerk dynamics. Figure 10 presents an analog circuit for the proposed system, where our circuit includes three analog multipliers, 12 resistors, 3 capacitors and 5 operational amplifiers.

We derive the mathematical equations of the circuit in Figure 10 using Kirchchoff's circuit laws as given below:

$$\begin{aligned} \dot{z_1} &= \tfrac{1}{C_1 R_1} z_2 \\ \dot{z_2} &= \tfrac{1}{C_2 R_2} z_3 \\ \dot{z_3} &= -\tfrac{1}{C_3 R_3} z_1 + \tfrac{1}{C_3 R_4} z_2 - \tfrac{1}{C_3 R_5} z_3 \\ &\quad - \tfrac{1}{10 C_3 R_6} z_1^2 - \tfrac{1}{10 C_3 R_7} z_1 z_2 + \tfrac{1}{10 C_3 R_8} z_2^2 \end{aligned} \tag{20}$$

Table 1 prescribes the values of the parts in the 5-D circuit (20).

Figures 11, 12 and 13 provide Multisim plots of the 3-D jerk circuit (20).

5 FPGA-based hardware implementation of the new chaotic jerk system

In this section, we detail the FPGA-based implementation of the chaotic jerk system (21). The first-order Euler method is used to calculate the numerical solution of the system (21).

Table 1 The Values of the Circuit Components in the 3-D Circuit (20)

Circuit Component	Value
R_4	$500k\Omega$
R_6	$50k\Omega$
R_7, R_8	$10k\Omega$
R_1, R_2, R_3, R_5	$100k\Omega$
$R_9, R_{10}, R_{11}, R_{12}$	$100k\Omega$
C_1, C_2, C_3	$1nF$
The power supplies	± 15 Volts

The experimental realization is made on the Xilinx Zynq-7000 XC7Z020 board. This board comprises a Xilinx 7-series Programmable Logic (PL) that is equivalent to an Artix-7 FPGA.

$$\begin{aligned} \dot{z}_1 &= z_2, \\ \dot{z}_2 &= z_3, \\ \dot{z}_3 &= -a z_1 + b z_2 - z_3 - c z_1^2 - z_1 z_2 + d z_2^2 \end{aligned} \tag{21}$$

The parameter values are assumed as follows:

$$a = 1,\ b = 0.2,\ c = 0.2,\ d = 1. \tag{22}$$

Figure 14 presents the methodology for the FPGA-based design of the chaotic jerk dynamics (Tlelo-Cuautle et al., 2016). First, the chaotic jerk system is simulated

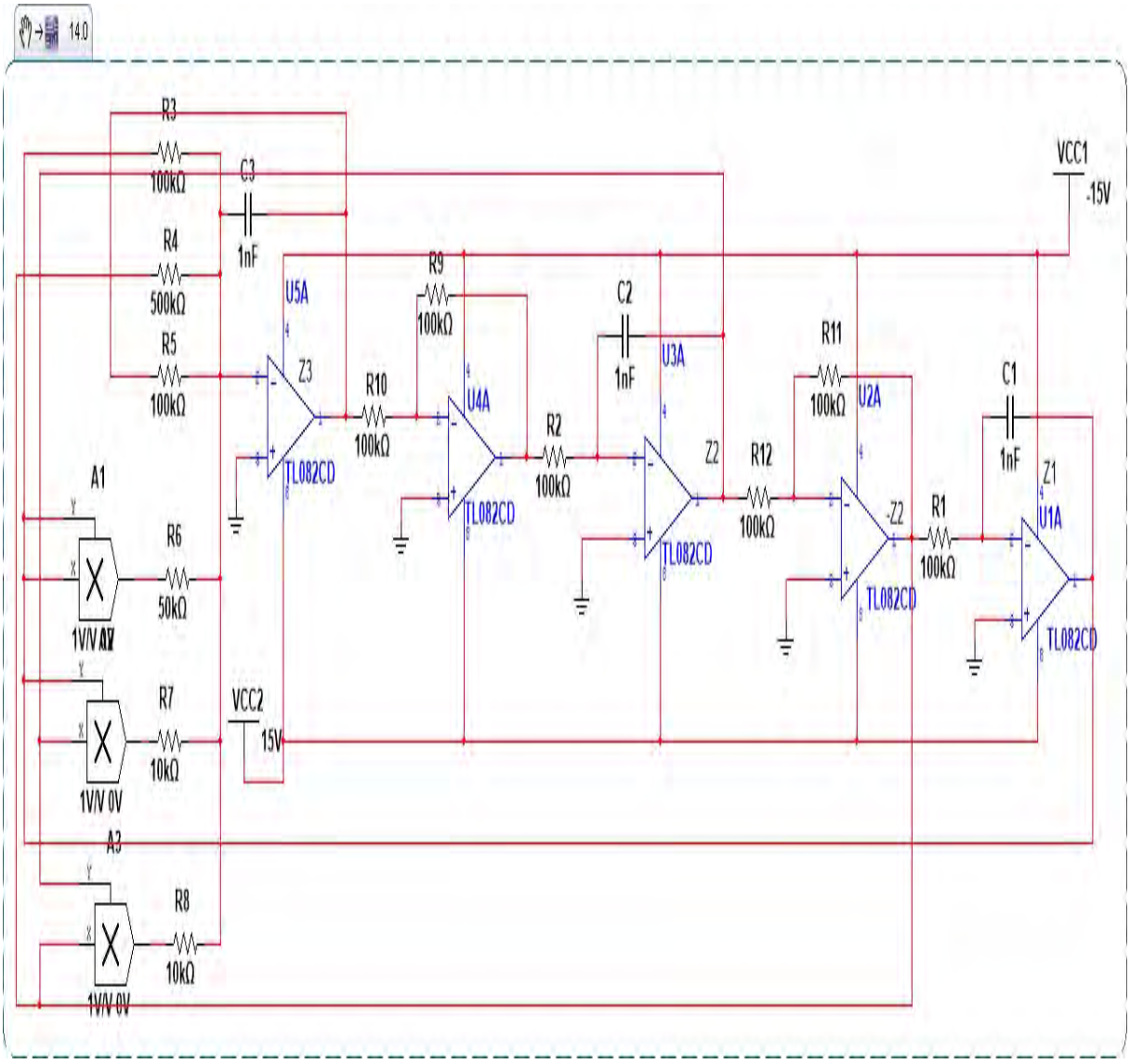

Figure 10: Circuit Design of the new 3-D chaotic jerk circuit (20)

.

using simple or double Floating-point precision in a mathematical environment such as Matlab or Python, then, the range for the numerical values is obtained. Next, the number of bits for representing such numerical values are obtained, herein the Fixed-point format representation $Q_{I,nI}$ is used, where I is the number of bits for the integer representation as well as the sign bit. Also, nI is the number of bits for non-integer representation. In the next step, the bit-width estimated from previous point is validated through numerical simulations. Finally, the solution of the system is implemented into the FPGA by using a Hardware Description Language like a VHDL or Verilog.

Further details of the flowchart described in Figure 14 are described below.

1. **Numerical Simulation in Floating-Point**.

   The algorithm in Figure 15 presents the pseudo-code for solving the chaotic jerk system with the Euler method whereas Figures 16, 17 and 18 depict the numerical simulation of the chaotic jerk system (21 elaborated in Python programming language.

   The range for each of the state variables of the chaotic jerk system (21) can be estimated from the numerical simulations of Figures 16-18 as follows:

   - $z_1 \in [-5, 35\,]$,
   - $z_2 \in [-25, 30\,]$,
   - $z_3 \in [-150, 120\,]$,

   As a result, the equations of the chaotic jerk system must be conveniently evaluated. Considering that $\max|\dot{z}_3| > \max|\dot{z}_2|, \max|\dot{z}_1|$, then the value for $\max|\dot{z}_3|$ is obtained by setting $(z_1, z_2, z_3) = (-5, 30, -150)$ as follows:

   $$\dot{z}_3 = 1206 \tag{23}$$

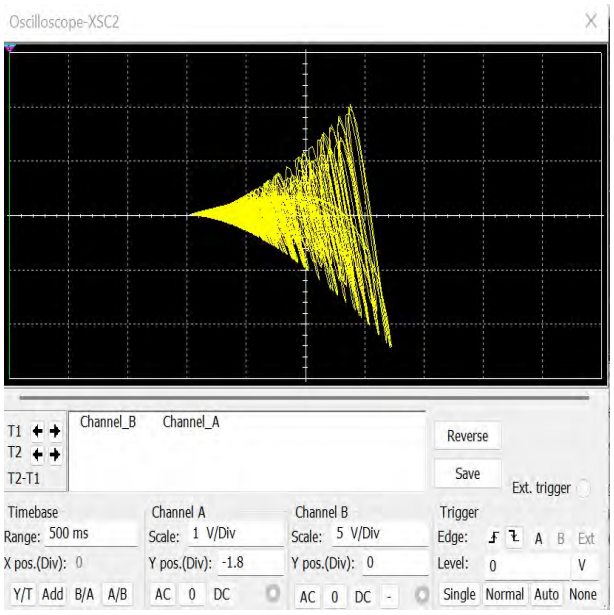

Figure 11: Multisim signal plot for the 3-D jerk circuit (20) in (z_1, z_2) plane

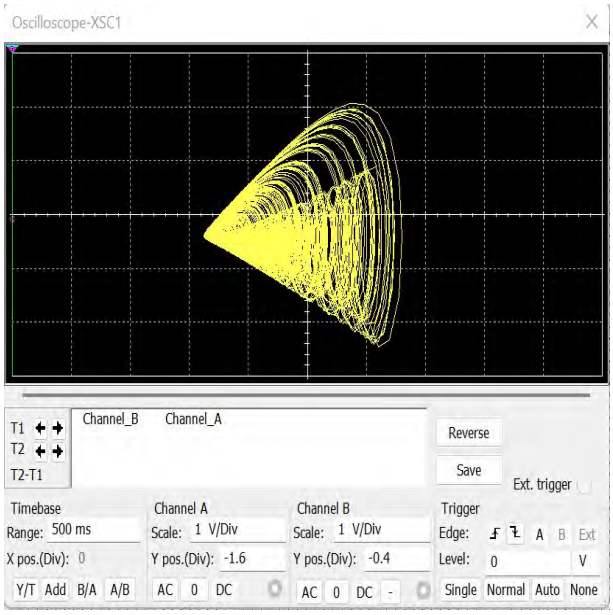

Figure 13: Multisim signal plot for the 3-D jerk circuit (20) in (z_1, z_3) plane

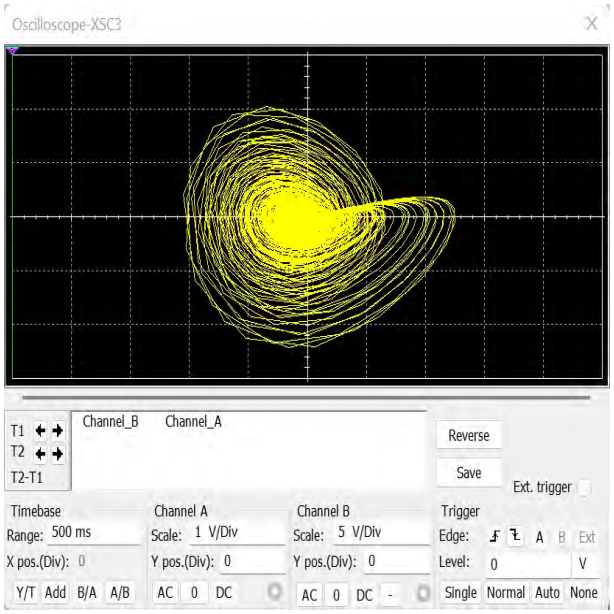

Figure 12: Multisim signal plot for the 3-D jerk circuit (20) in (z_2, z_3) plane

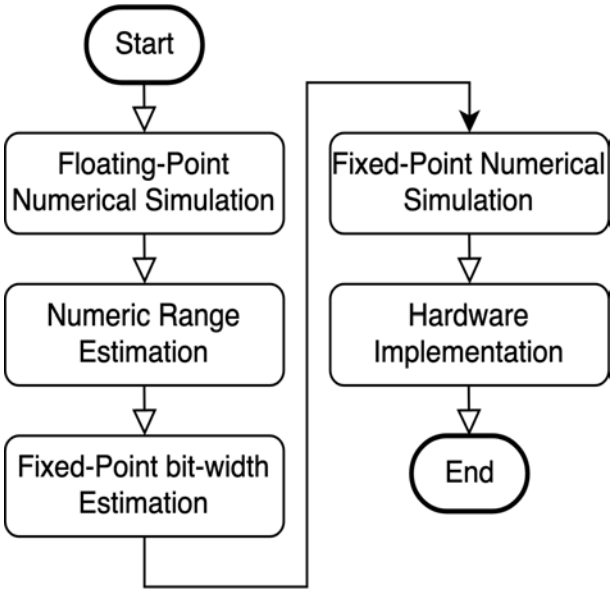

Figure 14: Flowchart for the FPGA-based implementation of the chaotic jerk system (21).

2. **Fixed-Point bit-width Estimation**.

   From equation (23) is observed that the maximum integer value to be represented is 1206, then, the necessary number of bits can be estimated as follows:

$$\lceil \log_2(1206) \rceil = 11, \tag{24}$$

   where $\lceil \cdot \rceil$ denotes the ceiling function.

   Then, the necessary number of bits are 11 + 1 (plus the sign bit). Considering that the FPGA design of this work is based on 32 bits computing operations, the remaining 20 bits can be used for the non integer part representation, so the Fixed-point format ends up being $Q_{11,20}$.

3. **Fixed-Point Numerical Simulation** The numerical simulation in the $Q_{11,20}$ Fixed-point format is made on C programming language by using integer operations. The algorithm in Fig. 22 gives the used pseudo-code for the numerical simulation, where the MUL$(\cdot)$ function performs the Fixed-Point multiplication of two numbers $Q_{11,20}$ with the whole inputs in Fixed-Point format.

Algorithm 1: Pseudocode for solving the chaotic jerk system with the Euler method.

Input: Parameters: $a = 1, b = 0.2, c = 0.2, d = 1,$

Initial conditions: $\big(z_1(t_0), z_2(t_0), z_3(t_0)\big) = (0.4, 0.1, 0.4),$

Step size: $h = 0.0015,$

while *True* **do**

$k1a = z_2(t_0)$

$k1b = z_3(t_0),$

$k1c = -az_1(t_0) + bz_2(t_0) - z_3(t_0) - cz_1(t_0)z_1(t_0) - z_1(t_0)z_2(t_0) + dz_2(t_0)z_2(t_0),$

Compute the solution:

$z_1 = z_1(t_0) + hk1a$

$z_2 = z_2(t_0) + hk1b$

$z_3 = z_3(t_0) + hk1c$

Replace initial conditions:

$z_1(t_0) \leftarrow z_1$

$z_2(t_0) \leftarrow z_2$

$z_3(t_0) \leftarrow z_3$

Output: z_1, z_2, z_3, z_4

Figure 15: Pseudocode for solving the chaotic jerk system (21) with the Euler method.

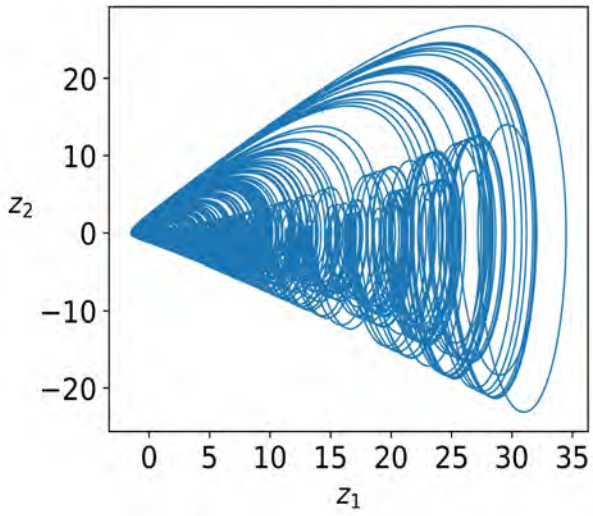

Figure 16: Numerical simulation of the chaotic jerk system (21) in (z_1, z_2) plane with step size $h = 0.0015$, simulation time $T_{sim} = 1800s$ and $Z(0) = (0.4, 0.1, 0.4)$.

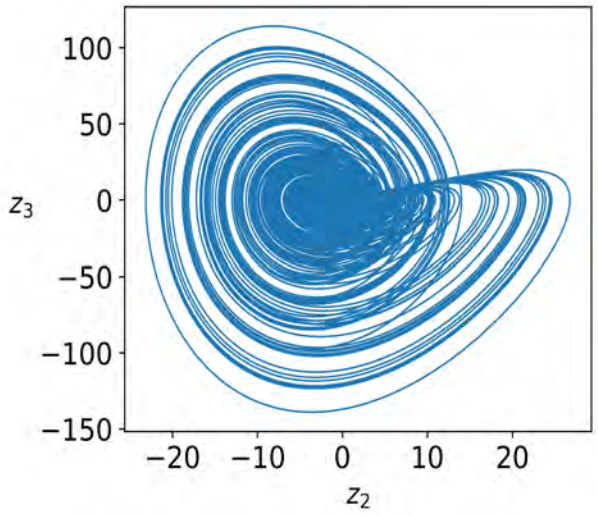

Figure 17: Numerical simulation of the chaotic jerk system (21) in (z_2, z_3) plane with step size $h = 0.0015$, simulation time $T_{sim} = 1800s$ and $Z(0) = (0.4, 0.1, 0.4)$.

Figures 19-21 display the numerical simulation results. The observed phase portraits agree with those obtained in Figures 16-18 since they converge to the same chaotic jerk attractor (21). Hence, the chosen fixed point format is selected for the FPGA implementation.

4. **Hardware Implementation.** The FPGA-based implementation of the chaotic jerk system is

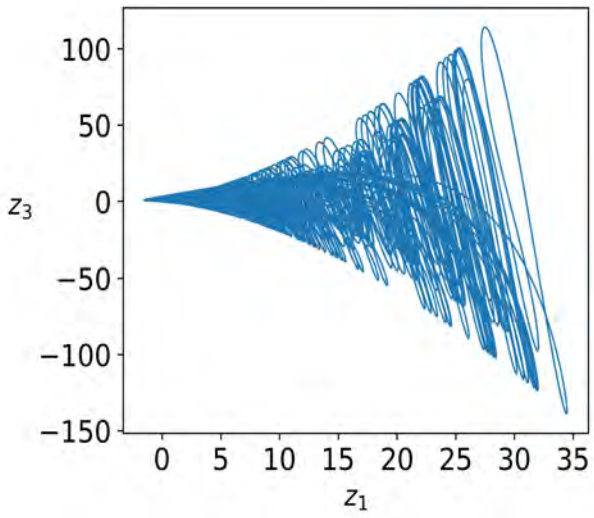

Figure 18: Numerical simulation of the chaotic jerk system (21) in (z_1, z_3) plane with step size $h = 0.0015$, simulation time $T_{sim} = 1800s$ and $Z(0) = (0.4, 0.1, 0.4)$.

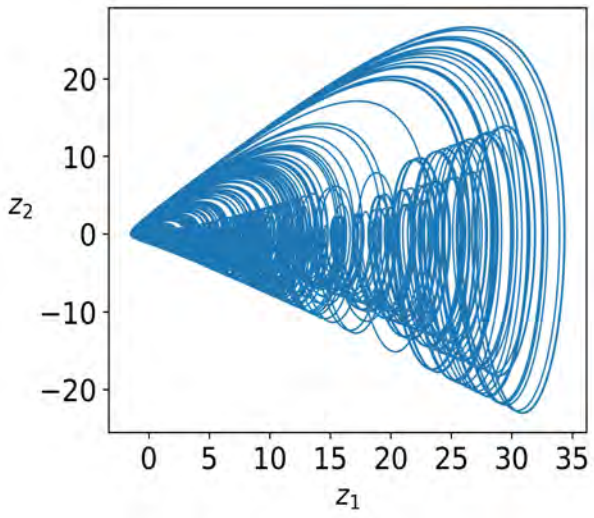

Figure 19: Numerical simulation on $Q_{11,20}$ fixed point format of the chaotic jerk system (21) in (z_1, z_2) plane with step size $h = 0.0015$, simulation time $T_{sim} = 1800s$ and $Z(0) = (0.4, 0.1, 0.4)$.

performed on the FPGA of the Xilinx Zynq-7000 employing VHDL for hardware configuration. Since the FPGA-based implementation is quite similar to the pseudo-code 22, we need to describe multipliers, adders and substractors in the VHDL enviroment.

Figure 23 shows the RTL schematic of the FPGA design of the chaotic jerk dynamics (21). It can be seen that the highest level description of the proposed block design comprises 5 blocks. Each block has its own Arithmetic Logic Unit (ALU) for performing separately calculations. In summary, the blocks labeled as z1_sol, z2_sol, z3_sol are responsible for calculating the numerical solution

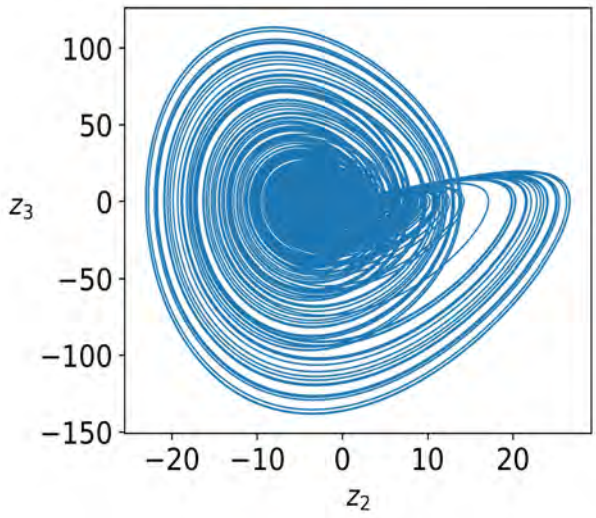

Figure 20: Numerical simulation on $Q_{11,20}$ fixed point format of the chaotic jerk system (21) in (z_2, z_3) plane with step size $h = 0.0015$, simulation time $T_{sim} = 1800s$ and $Z(0) = (0.4, 0.1, 0.4)$.

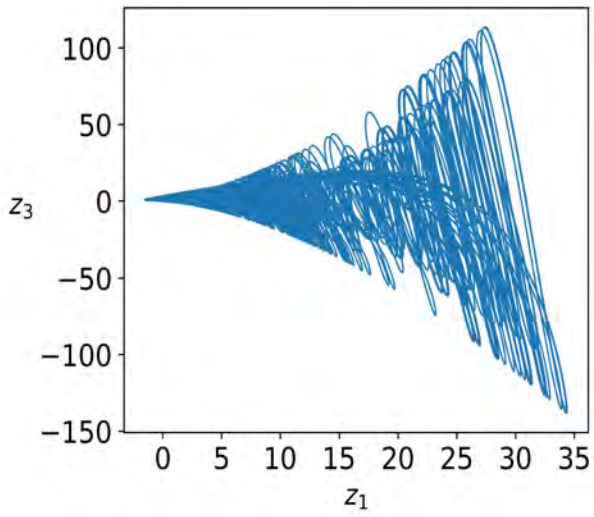

Figure 21: Numerical simulation on $Q_{11,20}$ fixed point format of the chaotic jerk system (21) in (z_1, z_3) plane with step size $h = 0.0015$, simulation time $T_{sim} = 1800s$ and $Z(0) = (0.4, 0.1, 0.4)$.

of the system variables whereas the block namely "Data_transition" is devoted for updating initial conditions.

Moreover, the "Data_transition" block is also responsible for sending the necessary data to the MCP4922_driver block, which is the SPI interface around for controlling a 12 bits dual-channel D/A converter MCP4922. We note that the SPI interface serves only for the experimental observation. Thus, the SPI interface should not be considered as part of the final FPGA design.

For a suitable visualization of the chaotic attractor, the post-processing technique depicted in Eq.

Algorithm 2: Fixed-Point pseudocode for solving the chaotic jerk system.

Input: Parameters: $a = 0x00100000$, $b = 0x00033333$, $c = 0x00033333$, $d = 0x00100000$,
Initial conditions: $(z_1(t_0), z_2(t_0), z_3(t_0)) = (0x00066666, 0x00019999, 0x00066666)$,
Step size: $h = 0x00000624$,
while *True* **do**

$k1a = \mathrm{MUL}(h, z_2(t_0))$

$k1b = \mathrm{MUL}(h, z_3(t_0))$

$R1 = \mathrm{MUL}(a, z_1(t_0))$
$R2 = \mathrm{MUL}(b, z_2(t_0))$
$R3 = \mathrm{MUL}(z_1(t_0), z_2(t_0))$
$R4 = \mathrm{MUL}(z_1(t_0), z_1(t_0))$
$R5 = \mathrm{MUL}(z_2(t_0), z_2(t_0))$
$R6 = \mathrm{MUL}(c, R4)$
$R7 = \mathrm{MUL}(d, R5)$
$R8 = R2 + R7 - R1 - R3 - R6 - z_3(t_0)$
$k1c = \mathrm{MUL}(h, R8)$

Compute the solution:
$z_1 = z_1(t_0) + k1a$

$z_2 = z_2(t_0) + k1b$

$z_3 = z_3(t_0) + k1c$

Replace initial conditions:
$z_1(t_0) \leftarrow z_1$
$z_2(t_0) \leftarrow z_2$
$z_3(t_0) \leftarrow z_3$

Output: z_1, z_2, z_3

Figure 22: Fixed-Point pseudocode for solving the chaotic jerk system (21)

(25) have been implemented on the block namely "Data_transition" of Figure 23. Later, the 12 bits dual-channel digital to analog (D/A) converter MCP4922 is used for the D/A of the chaotic sequences, the experimental results are observed on a Tektronix DPO2022B oscilloscope.

$$\begin{aligned}
&\text{dac_data_ch0} = \lceil m_1 \times \text{z1out} \rceil + \sigma_1, \\
&\text{dac_data_ch1} = \lceil m_2 \times \text{z2out} \rceil + \sigma_2, \\
&\qquad\qquad \text{or} \\
&\text{dac_data_ch0} = \lceil m_2 \times \text{z2out} \rceil + \sigma_2, \\
&\text{dac_data_ch1} = \lceil m_3 \times \text{z3out} \rceil + \sigma_3, \\
&\qquad\qquad \text{or} \\
&\text{dac_data_ch0} = \lceil m_1 \times \text{z1out} \rceil + \sigma_1, \\
&\text{dac_data_ch1} = \lceil m_3 \times \text{z3out} \rceil + \sigma_3
\end{aligned} \tag{25}$$

where $\text{z1out}, \text{z2out}, \text{z3out} \in N^+$, $(m_1, m_2, m_3) = (110, 80, 16)$ and $(\sigma_1, \sigma_2, \sigma_3) = (200, 1900, 2250)$.

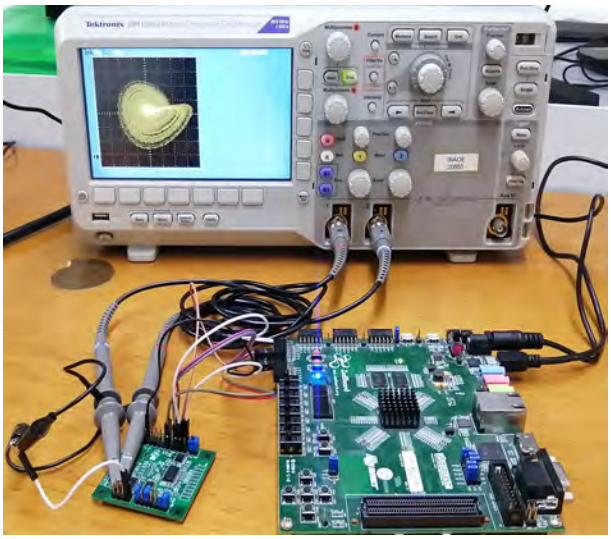

Figure 24: Experimental setup for the implementation of the chaotic jerk system.

Figure 24 shows the experimental setup for the FPGA-based implementation of the chaotic jerk system. Finally, Figures 25-27 present the experimental phase portraits, which are clearly consistent with those obtained by numerical simulations in Figures 16-18 and Figures 19- 21.

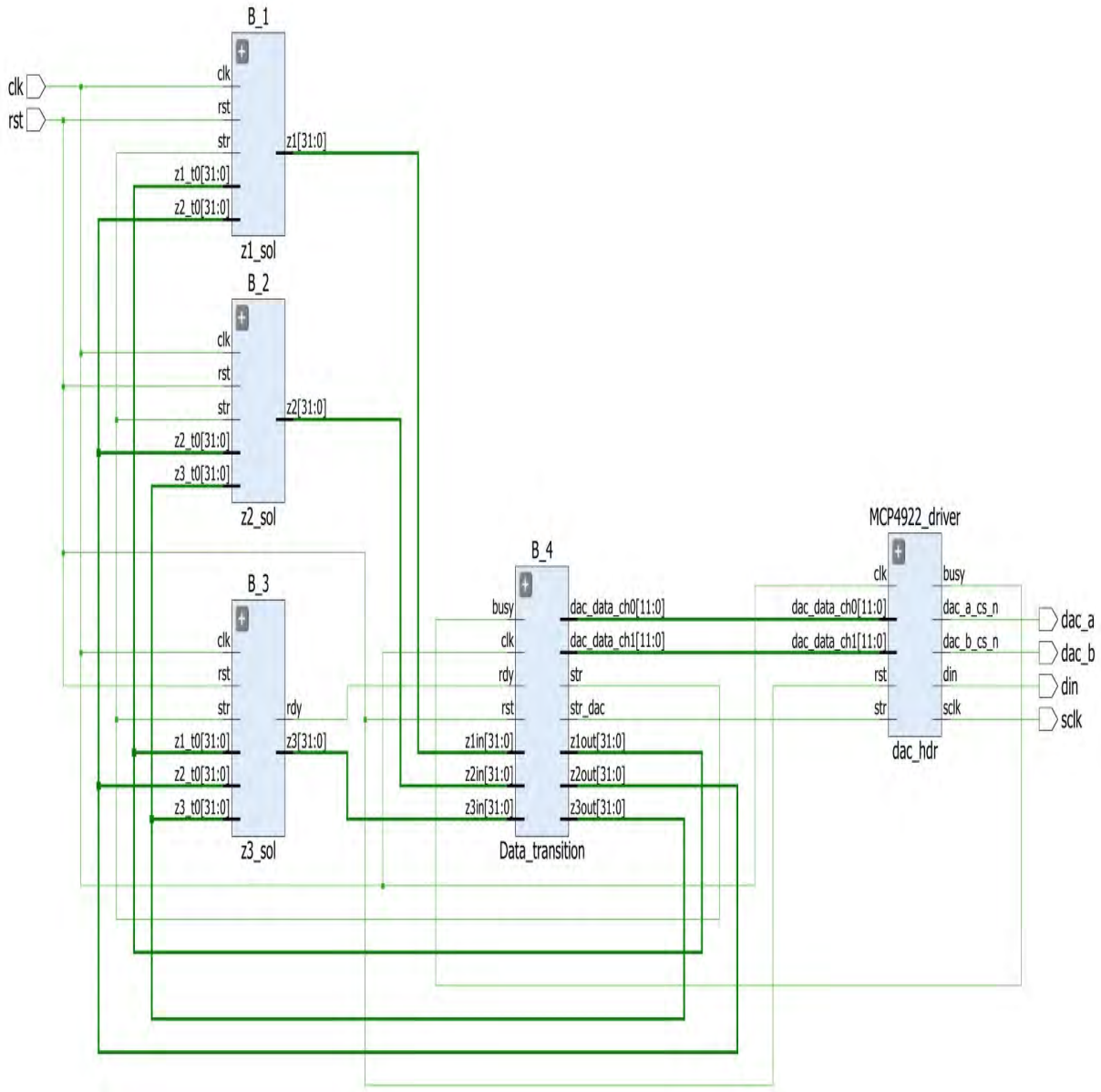

Figure 23: RTL schematics of the FPGA-based implementation for the chaotic jerk system (21)

In Table 2, we present the hardware resources utilization by the FPGA implementation. In general, the implementation have a low hardware cost. It can be seen that DSPs are the most utilized resources, consuming up to 12.73 % of the total available, which is a trade-off for the parallel computing configuration. In Table 3, we show the performance of the FPGA implementation, which at the current state has a clock frequency of 106.382 MHz and a throughput of 3.404 Gbit/s. Finally, in Figure 28, we observe that the proposed FPGA design has a total power consumption of $0.2W$.

Table 2 Resources utilization of the FPGA design of the chaotic jerk dynamics (21).

Resource	Available	Used
LUT	53200	635 (1.19 %)
FF	106400	747 (0.70%)
DSP	220	28 (12.73%)
IO	200	98 (49.00 %)
BUFG	32	1 (3.13 %)

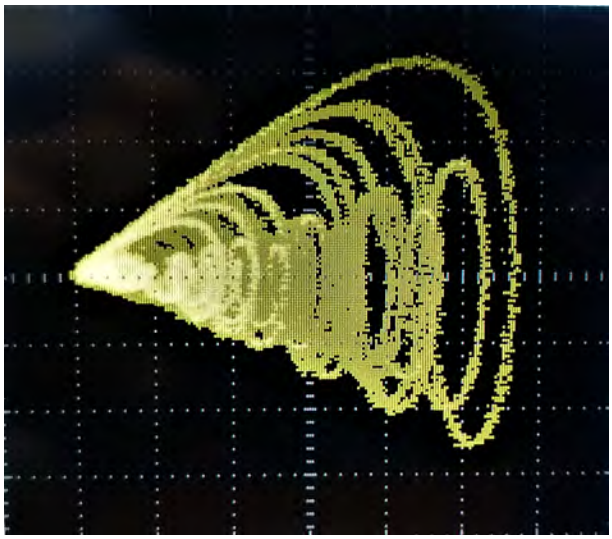

Figure 25: Phase portrait of the experimental results of the chaotic jerk system (21) in (z_1, z_2) plane

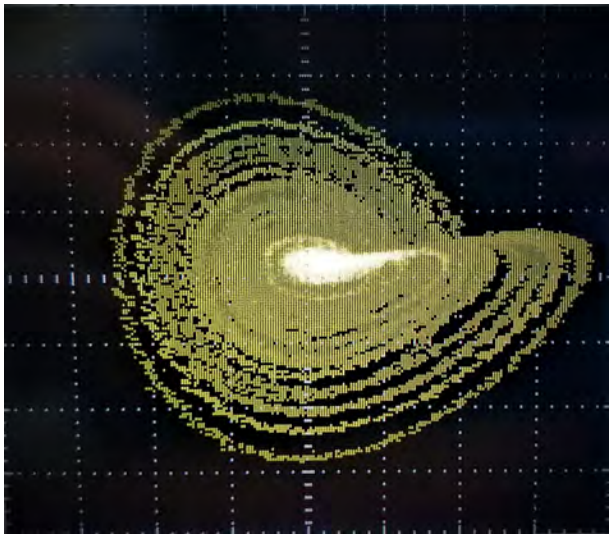

Figure 26: Phase portrait of the experimental results of the chaotic jerk system (21) in (z_2, z_3) plane

Table 3 Performance results of the FPGA design of the chaotic jerk dynamics (21).

Clock frequency	106.382 MHz
Throughput	3.404 Gbit/s

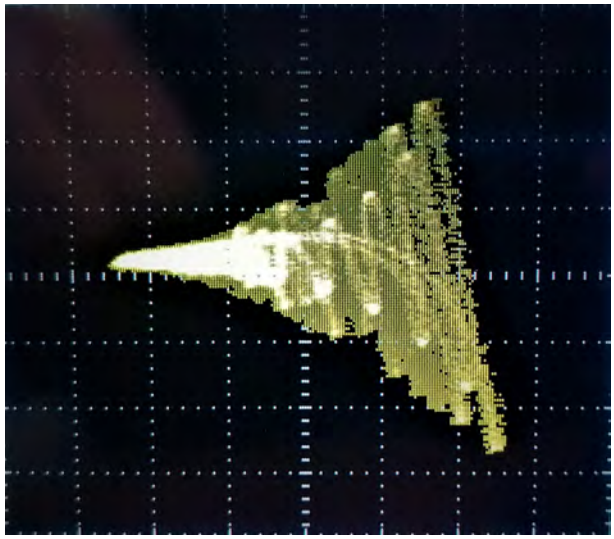

Figure 27: Phase portrait of the experimental results of the chaotic jerk system (21) in (z_1, z_3) plane

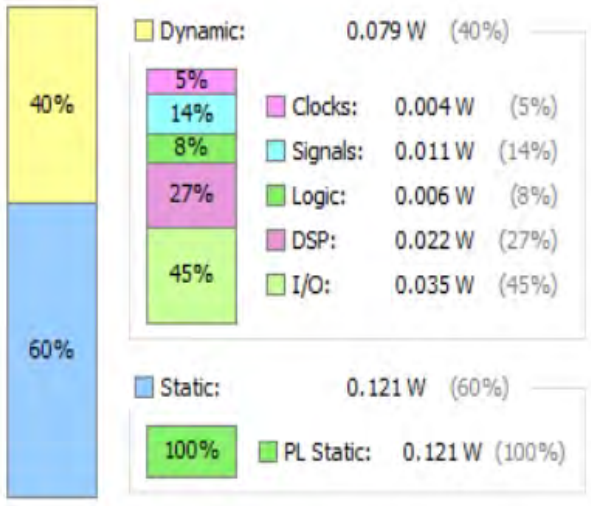

Figure 28: Power consumption of the FPGA design of the chaotic jerk system (21)

6 Conclusions

We reported a new 3-D mechanical chaotic system with a jerk dynamics and a self-excited chaotic attractor. We showed that the new jerk dynamics exhibits Hopf bifurcations associated with the unstable balance points for certain values of the system parameters. We showed that the new jerk system has coexisting chaotic attractors and multi-stability. Using Multisim (Version 14), an electronic circuit was designed for the proposed mechanical chaotic system with jerk dynamics. As another engineering application, Field Programmable Gate Array (FPGA) design was made for the proposed mechanical jerk chaotic system. Euler's finite-difference method is used for our FPGA design. An experimental implementation of the FPGA-based design was performed in this work and experimental results such as performance analysis, power consumption, etc. were given in detail.

References

Abdullah, H. A. and Mohammed, R. K. (2022). Fpga-based modified chaotic system for speech transmission.

International Journal of Speech Technology, 25(3):651 – 657.

Al-Basyouni, K. and Khan, A. (2022). Discrete-time covid-19 epidemic model with chaos, stability and bifurcation. *Results in Physics*, 43. Article ID 106038.

Anandkumar, R. and Kalpana, R. (2022). A Fibonacci p-code traversing and unified chaotic map-based image encryption algorithm. *Journal of Ambient Intelligence and Humanized Computing*, 13(8):3713 – 3727.

Arowolo, M. O., Awotunde, J. B., Ayegba, P., and Haroon-Sulyman, S. O. (2022). Relevant gene selection using ANOVA-ant colony optimisation approach for malaria vector data classification. *International Journal of Modelling, Identification and Control*, 41(1 - 2):12 – 21.

Bors, D. and Stańczy, R. (2023). Dynamical system describing cloud of particles. *Journal of Differential Equations*, 342:21 – 33.

Cao, K. and Lai, Q. (2022). A simple memristive chaotic system with complex dynamics and ITS image encryption application. *International Journal of Modern Physics B*, 36(21). Article ID 2250131.

Chen, C. and Min, F. (2022). Memristive bi-neuron hopfield neural network with coexisting symmetric behaviors. *European Physical Journal Plus*, 137(7). Article ID 841.

Das, A. and Mohanty, M. N. (2022a). Classification of magnetic resonance images of brain using concatenated deep neural network. *International Journal of Modelling, Identification and Control*, 41(1 - 2):4 – 11.

Das, A. and Mohanty, M. N. (2022b). An improved ensemble learning approach for the prediction of cardiovascular disease using majority voting prediction. *International Journal of Modelling, Identification and Control*, 41(1 - 2):68–86.

Dilna, K., Anitha, J., and Hemanth, D. J. (2022). A novel framework for segmentation of uterus fibroids in ultrasound images using machine learning models. *International Journal of Modelling, Identification and Control*, 41(1 - 2):22 – 31.

Dong, Q., Zhou, S., Zhang, Q., and Kasabov, N. K. (2022). A class of 5d hamiltonian conservative hyperchaotic systems with symmetry and multistability. *Nonlinear Dynamics*, 110(3):2889 – 2912.

Farlessyost, W. and Singh, S. (2022). Reduced order dynamical models for complex dynamics in manufacturing and natural systems using machine learning. *Nonlinear Dynamics*, 110(2):1613 – 1631.

Guckenheimer, J. and Holmes, P. (1983). *Nonlinear Oscillations, Dynamical Systems and Bifurcations of Vector Fields*. Springer, New York.

Guo, W. and Li, W. (2023). Simulating vibrations of two-wheeled self-balanced robots with road excitations by MATLAB. *Mechanisms and Machine Science*, 123:51 – 68.

Gupta, J., Dhar, J., and Sinha, P. (2023). Infection dynamics of rabbit and red fox with alternative prey. *Journal of Mathematics and Computer Science*, 29(3):214 – 238.

Gupta, M. D. and Chauhan, R. (2022). Hardware efficient pseudo-random number generator using chen chaotic system on fpga. *Journal of Circuits, Systems and Computers*, 31(3). Article ID 2250043.

Han, X. and Lei, C. (2023). Bifurcation and turing instability analysis for a space- and time-discrete predator–prey system with smith growth function. *Chaos, Solitons and Fractals*, 166. Article ID 112910.

Hassani, I., Maalej, I., and Rekik, C. (2022). Control points searching algorithm for multiple mobile robots. *International Journal of Modelling, Identification and Control*, 41(1 - 2):120 – 132.

Hide, R., Skeldon, A. C., and Acheson, D. J. (1996). A study of two novel self-exciting single-diesk homopolar dynamos: theory. *Proc. R. Lond. A*, 452:1369 – 1395.

Kengne, L. K., Muni, S. S., Chedjou, J. C., and Kyandoghere, K. (2022). Various coexisting attractors, asymmetry analysis and multistability control in a 3d memristive jerk system. *European Physical Journal Plus*, 137(7). Article ID 848.

Li, A. and Sun, J. (2023). Resource limited event-triggered model predictive control for continuous-time nonlinear systems based on first-order hold. *Nonlinear Analysis: Hybrid Systems*, 47. Article ID 101273.

Li, C.-B. and Ye, Y.-L. (2023). A comparison of topological entropies for nonautonomous dynamical systems. *Journal of Mathematical Analysis and Applications*, 517(2). Article ID 126627.

Li, J. and Cui, N. (2023). A hyperchaos generated from rabinovich system. *AIMS Mathematics*, 8(1):1410 – 1426.

Liu, C.-S. and Chang, C.-W. (2023). Periodic solutions of nonlinear ordinary differential equations computed by a boundary shape function method and a generalized derivative-free Newton method. *Mechanical Systems and Signal Processing*, 184. Article ID 109712.

Liu, L. and Wang, J. (2023). A cluster of 1D quadratic chaotic map and its applications in image encryption. *Mathematics and Computers in Simulation*, 204:89 – 114.

Mao, X. and Lei, F. (2022). Stability analysis and coexisting behaviors of a delayed multiplex network under electromagnetic radiation. *International Journal of Bifurcation and Chaos*, 32(10). Article ID 2250148.

Mastrone, M. N. and Co, F. (2023). Numerical modeling of fluid's aeration: Analysis of the power losses and lubricant distribution in gearboxes. *Journal of Applied and Computational Mechanics*, 9(1):83 – 94.

Nagase, K. and Taniuchi, K. (2023). Wave analysis and control of uniformly varying two-dimensional ladder-network structures. *Mechanical Systems and Signal Processing*, 185. Article ID109765.

Ostrovskii, V. Y., Rybin, V. G., Karimov, A. I., and Butusov, D. N. (2022). Inducing multistability in discrete chaotic systems using numerical integration with variable symmetry. *Chaos, Solitons and Fractals*, 165. Article ID 112794.

Owais, R. and Iqbal, S. J. (2022). Sensorless DC-link voltage regulation strategy for single-phase grid-connected solar photovoltaic systems. *International Journal of Modelling, Identification and Control*, 41(1 - 2):133 – 142.

Patro, S. P., Padhy, N., and Sah, R. D. (2022). An improved ensemble learning approach for the prediction of cardiovascular disease using majority voting prediction. *International Journal of Modelling, Identification and Control*, 41(1 - 2):4 – 11.

Rech, P. C. (2022). Self-excited and hidden attractors in a multistable jerk system. *Chaos, Solitons and Fractals*, 164. Article ID 112614.

Ryashko, L. (2022). Noise-induced multirhythmicity, bursting, and order-chaos transitions in the 3D Goldbeter system. *International Journal of Bifurcation and Chaos*, 32(10). Article ID 2250157.

Sachin and Singh, P. (2022). A novel chaotic umbrella map and its application to image encryption. *Optical and Quantum Electronics*, 54(5). Article ID 266.

Samuilik, I. and Sadyrbaev, F. (2023). On a dynamical model of genetic networks. *WSEAS Transactions on Business and Economics*, 20:104 – 112.

Shafaei, S. and Mousazadeh, H. (2023). Parametric analysis of traction energy of an autonomous wheeled robotic system for application in greenhouse environment. *Journal of Terramechanics*, 105:11 – 25.

Shafique, A. (2022). A noise-tolerant cryptosystem based on the decomposition of bit-planes and the analysis of chaotic gauss iterated map. *Neural Computing and Applications*, 34(19):16805 – 16828.

Singh, A. and Rai, S. K. (2022). OTA and CDTA-based new memristor-less meminductor emulators and their applications. *Journal of Computational Electronics*, 21(4):1026 – 1037.

Sui, G. and Zhang, Y. (2023). Response spectrum method for fatigue damage assessment of mechanical systems. *International Journal of Fatigue*, 166. Article ID 107278.

Tagne, S., Bodo, B., Eyebe, G. F. V. A., and Fouda, J. S. A. E. (2022). Pic micro-controller based synchronization of two fractional order jerk systems. *Scientific Reports*, 12(1). Article ID 14281.

Thounaojam, U. S. (2022). Stochastic chaos in chemical Lorenz system: Interplay of intrinsic noise and nonlinearity. *Chaos, Solitons and Fractals*, 165. Article ID 112763.

Tlelo-Cuautle, E., De la Fraga, L., and Rangel-Magdaleno, J. (2016). *Engineering applications of FPGAs*. Springer.

Törk, Ö. (2022). Fpga simulation of chaotic tent map-based s-box design. *International Journal of Circuit Theory and Applications*, 50(5):1589 – 1603.

Vaidyanathan, S., Akgul, A., and Kacar, S. (2018). A new chaotic jerk system with two quadratic nonlinearities and its applications to electronic circuit implementation and image encryption. *International Journal of Computer Applications in Technology*, 58(2):89 – 101.

Wang, F.-B. and Cheng, C.-Y. (2021). A diffusive virus model with a fixed intracellular delay and combined drug treatments. *Journal of Mathematical Biology*, 83(2). Article ID 19.

Wang, J. and Yang, C. (2021). Chaos synchronization of a finance chaotic system with an integral sliding mode controller. *Journal of Mathematics*, 2021. Article ID 6611031.

Wang, Y., Li, Y., Xu, C., and Shi, C. (2022). Map matching navigation method based on scene information fusion. *International Journal of Modelling, Identification and Control*, 41(1 - 2):110 – 119.

Wang, Z. and Guet, C. (2022). Self-consistent learning of neural dynamical systems from noisy time series. *IEEE Transactions on Emerging Topics in Computational Intelligence*, 6(5):1103 – 1112.

Wu, Q. and Chen, Y. (2023). Adaptive cooperative control of a soft elbow rehabilitation exoskeleton based on improved joint torque estimation. *Mechanical Systems and Signal Processing*, 184. Article ID 109748.

Xu, C. (2022). Washout filter control technique for a fractional-order chaotic finance model. *Ain Shams Engineering Journal*, 13(3). Article ID 101644.

Xu, L. and Zhang, J. (2022). A novel four-wing chaotic system with multiple attractors based on hyperbolic sine: Application to image encryption. *Integration*, 87:313 – 331.

Yu, M. and Zhang, Z. (2023). Optimal Liouville-type theorems for polyharmonic elliptic gradient systems and applications. *Journal of Mathematical Analysis and Applications*, 519(1). Article ID 126753.

Zhang, X. and Li, C. (2022). A novel type of chaotic attractor with a multiunit structure: From multiscroll attractors to multi-bond orbital attractors. *European Physical Journal Plus*, 137(9). Article ID 1048.

Zhen, L. and Hongbao, L. (2023). Influencing factors and mechanism of nanoparticle renal targeting. *Chinese Journal of Tissue Engineering Research*, 27(3):453 – 460.